

# Topological Phases in $\text{InAs}_{1-x}\text{Sb}_x$ : From Novel Topological Semimetal to Majorana Wire

Georg W. Winkler<sup>1</sup>, QuanSheng Wu<sup>1</sup>, Matthias Troyer<sup>1</sup>, Peter Krogstrup<sup>2</sup>, and Alexey A. Soluyanov<sup>1,3</sup>

<sup>1</sup>Theoretical Physics and Station Q Zurich, ETH Zurich, 8093 Zurich, Switzerland

<sup>2</sup>Center for Quantum Devices and Station Q Copenhagen, Niels Bohr Institute,  
University of Copenhagen, 2100 Copenhagen, Denmark and

<sup>3</sup>Department of Physics, St. Petersburg State University, St. Petersburg, 199034 Russia

(Dated: June 26, 2018)

Superconductor proximitized one-dimensional semiconductor nanowires with strong spin-orbit interaction (SOI) are at this time the most promising candidates for the realization of topological quantum information processing. In current experiments the SOI originates predominantly from extrinsic fields, induced by finite size effects and applied gate voltages. The dependence of the topological transition in these devices on microscopic details makes scaling to a large number of devices difficult unless a material with dominant intrinsic bulk SOI is used. Here we show that wires made of certain ordered alloys  $\text{InAs}_{1-x}\text{Sb}_x$  have spin splittings up to 20 times larger than those reached in pristine InSb wires. In particular, we show this for a stable ordered CuPt-structure at  $x = 0.5$ , which has an inverted band ordering and realizes a novel type of a topological semimetal with triple degeneracy points in the bulk spectrum that produce topological surface Fermi arcs. Experimentally achievable strains can drive this compound either into a topological insulator phase, or restore the normal band ordering making the CuPt-ordered  $\text{InAs}_{0.5}\text{Sb}_{0.5}$  a semiconductor with a large intrinsic linear in  $k$  bulk spin splitting.

In recent years, a range of topological phases have been realized in materials, ranging from topological insulators [1, 2] (TIs) and semimetals [3–6] (TSMs) to superconductors [7, 8] (TSCs). The non-trivial topology of the ground state wavefunctions in these phases causes a variety of phenomena in such materials ranging from topologically protected metallic surface or edge states in TIs [1, 2] and Fermi arcs and anomalous magnetotransport in TSMs [4, 9–11], to quasiparticles with non-Abelian particle statistics [12–19] in TSCs, which could be used for topological quantum computation [20, 21].

Arguably the simplest scheme for realizing non-Abelian statistics in a solid-state device is based on manipulating Majorana zero modes (MZMs) in networks of semiconductor wires. MZMs were predicted to appear at the ends of spin-orbit coupled wires subject to a parallel magnetic field, proximity coupled to an  $s$ -wave superconductor. Experimental observations, consistent with the theory, were reported for InAs and InSb zincblende nanowires [19, 22–24].

The stability of MZMs in such a setup depends greatly on the size of the spin-orbit splitting (SOS) of the conduction band. SOS is very small in bulk zincblende semiconductors [25] and the realization of the MZMs thus relies on the externally induced Rashba SOS [26], which is estimated to be of the order of 1 meV [27, 28]. This value is very small compared to the bulk splitting in some recently discovered compounds [29–32]. However, most of these materials are not suitable for realizing MZMs within the above scenario, while for others such experiments appear to be challenging. It is thus desirable to understand if large values of bulk SOS can be achieved within the III-V materials class, used in most experiments at this time. A bulk SOS dominating the Rashba

contributions would also make realization of MZMs far less sensitive to particular microscopic details of a specific device.

In this Letter we argue that certain *ordered* alloys with composition  $\text{InAs}_{1-x}\text{Sb}_x$  have sizable SOS and provide an optimal material for the realization of MZMs. For ternary alloys to give an advantage over fixed binary III-V compounds, SOS should be enhanced, ideally while preserving the high carrier mobility. We thus focus our attention on ordered superlattice structures. We find, in particular, that a CuPt-ordering with  $x = 0.5$  is energetically stable and hosts a *novel TSM phase*, which is identified as an interpolation of the established Dirac [33–35] and Weyl [4, 7] TSMs. Moreover, the TSM phase can be tuned either into a TI or normal insulator phase by application of strain. We also find that for the latter the spin-orbit energy  $E_{\text{SO}}$  [36] can be as large as 24 meV. Experimental evidence for the CuPt-ordering of  $\text{InAs}_{0.5}\text{Sb}_{0.5}$  exists [37–41], and we argue that nanowires of this structure can be grown with molecular beam epitaxy.

The SOS of the conduction band in zincblende structures is at most cubic in  $k$  around the  $\Gamma$ -point [25]. In both III-V materials, the conduction band has a minimum at  $\Gamma$  and an  $s$ -like character dictated by  $T_d$  symmetry. A SOS linear in  $k$  can thus only be achieved by breaking the  $T_d$  symmetry. We ask the question if there is a modification to the III-V materials, such that a bulk linear in  $k$  SOS is achieved.

*Disorder in nanoscale structures* — In the randomly disordered alloy  $\text{InAs}_{1-x}\text{Sb}_x$  any  $T_d$  symmetry breaking terms need to vanish because of averaging. However, in a nanoscale device, like a quantum dot or wire, the averaging will not be complete and a “bulk” contribution to the linear in  $k$  SOS is expected. We study this ef-

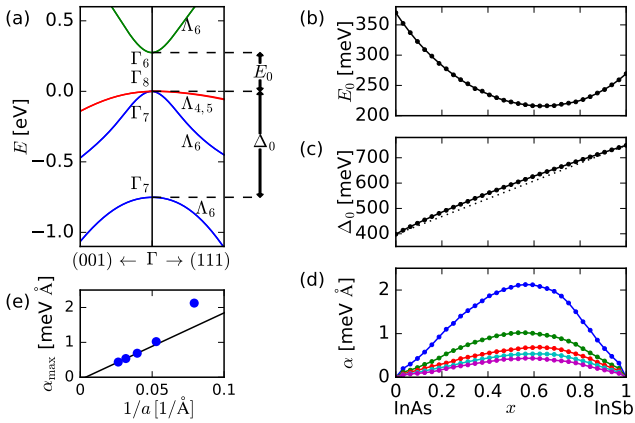


FIG. 1. (a): First-principles band structure of zincblende InSb around the  $\Gamma$  point, plotted up to  $|\mathbf{k}| = 0.1 \text{ \AA}^{-1}$ . Apart from the  $\Lambda_{4,5}$  representations each plotted band is two-fold degenerate. The next panels illustrate the change in the band structure of  $\text{InAs}_{1-x}\text{Sb}_x$  as a function of  $x$  obtained from ETB supercell calculations: (b) the fundamental gap  $E_0(x)$ , (c) the spin-orbit gap  $\Delta_0(x)$ , with the linear dotted line as a guide to show the bowing, and (d) the Rashba coefficient  $\alpha(x)$  of Eq. 1 for the SOS in the (110)-direction. Various supercell sizes are shown: 64 (blue), 216 (green), 512 (red), 1000 (cyan) and 1728 (magenta) atoms. (e) the maximum splitting  $\alpha_{\max}$  with linear extrapolation to an infinitely large cubic supercell.

fect by simulating randomly disordered cubic supercells of  $\text{InAs}_{1-x}\text{Sb}_x$  [42]. The supercell calculations are facilitated within Slater-Koster tight-binding models [43] of the  $sp^3s^*$  type [44–46], with parameters derived from first principles bulk calculations employing the HSE06 hybrid functional [47–50]. See Supplementary Material [51] for technical details on the calculation.

Figure 1 (b-c) show the composition dependence of the band gap  $E_0$  and the spin-orbit gap  $\Delta_0$ . The curves  $E_0(x)$  and  $\Delta_0(x)$  exhibit the correct bowing (non-linearity), and are in good agreement with recent experiments [52–54]. The linear in  $k$  SOS of the lowest conduction band is quantified by fitting the band structure calculations to an effective Hamiltonian

$$E_c^\pm(k) = \frac{\hbar^2 k^2}{2m^*} \pm \alpha k. \quad (1)$$

The parameter  $\alpha$  plays the role of the Rashba parameter in standard models for Majorana wires [15, 16, 18]. The magnitude of this coefficient varies with the  $k$ -space direction, and its dependence on disorder realizations is shown in Fig. 1(d) for the (110) direction [55]. As expected,  $\alpha$  decreases due to averaging when the supercell size is enlarged, which is also shown in Figure 1(e). As a consequence, wires or quantum dots of randomly alloyed  $\text{InAs}_{1-x}\text{Sb}_x$  have a universal bulk contribution to the SOS that depends strongly on the size of the device.

*CuPt-ordered structure* — In contrast to the disordered configurations above,  $T_d$  symmetry breaking by al-

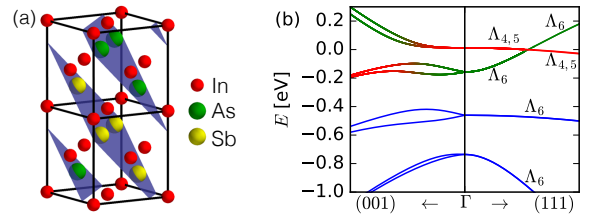


FIG. 2. (a) Crystal structure of CuPt-ordered  $\text{InAs}_{0.5}\text{Sb}_{0.5}$ . (b) Band structure of CuPt-ordered  $\text{InAs}_{0.5}\text{Sb}_{0.5}$  around  $\Gamma$  (plotted up to  $|\mathbf{k}| = 0.1 \text{ \AA}^{-1}$ ). The colors correspond to the original band ordering in Fig. 1.

loy ordering is nonvanishing for arbitrary system size. Since Fig. 1(d) shows that  $\alpha$  is maximized in the vicinity of  $x \approx 0.6$  we focus on small ordered supercells with  $x = 0.5$  as good candidates for realization of large SOS, maximizing  $E_{\text{SO}} = \frac{m^* \alpha^2}{2\hbar^2}$ . In particular, we considered three types of ordering reported in experiments on III-V ternary alloys [38]: ordering in  $\{100\}$  planes (CuAu-I or  $L1_0$  structure), ordering in  $\{210\}$  planes (chalcopyrite or  $E1_1$  structure) and ordering in  $\{111\}$  planes (CuPt or  $L1_1$  structure). The CuPt-type ordering is energetically stable in  $\text{InAs}_{0.5}\text{Sb}_{0.5}$  [51] and has been experimentally observed under various growth conditions [37–41]. We find that this structure also has the biggest enhancement of the SOS (see Supplementary Material [51]). We thus consider this type of ordering in the following.

In the CuPt-ordered  $\text{InAs}_{0.5}\text{Sb}_{0.5}$  structure, shown in Fig. 2(a), atoms of As and Sb are arranged in  $\{111\}$  planes that grow in the alternating order In-As-In-Sb. This ordering reduces the  $T_d$  (space group #216) symmetry of the pristine zincblende compounds to  $C_{3v}$  (space group #160), that has a three-fold rotational axis coinciding with the (111) direction, and three vertical mirror planes that contain the symmetry axis and are rotated by  $2\pi/3$  relative to each other. Both the ionic positions and lattice vectors were relaxed using the HSE06 hybrid functional to get the lowest energy structure. We found the deviation from the cubic structure to be smaller than 0.1% [51].

The band structure of CuPt-ordered  $\text{InAs}_{0.5}\text{Sb}_{0.5}$  obtained with HSE06 is shown in Fig. 2(b). The little group of  $k$ -points on the (111)-axis in the CuPt-structure is  $C_{3v}$  as in the zincblende structure, hence the same symmetry label  $\Lambda$  is used for the bands in Figs. 1(a) and 2(b). While the  $\Lambda_{4,5}$  bands have a very small, linear in  $k$ , splitting, the bands of the  $\Lambda_6$  representation are doubly degenerate. Note that the ordering of the valence and conduction bands at  $\Gamma$  is interchanged for the two structures, resulting in a *band inversion* in the CuPt-structure. We find the band inversion to be stable against deviations from the CuPt-order, in particular we find that CuPt-ordered  $\text{InAs}_{0.67}\text{Sb}_{0.33}$  and  $\text{InAs}_{0.33}\text{Sb}_{0.67}$  still show a strong band inversion [51].

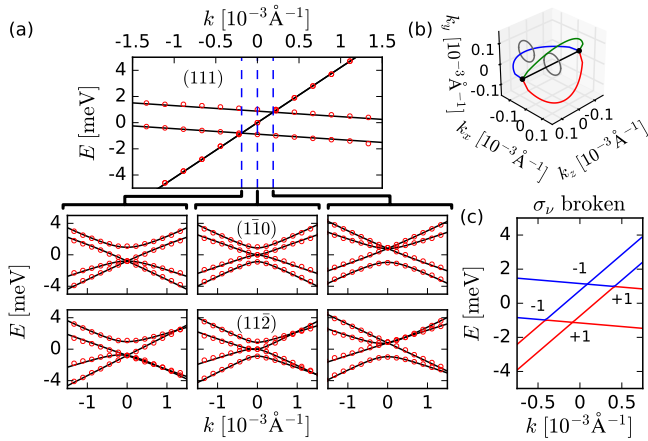


FIG. 3. (a) Zoom in of the TP for the three orthogonal  $k$ -directions and at three different values of momentum along the (111) direction. Band structures obtained from both first-principles calculations (red dots) and the  $\mathbf{k}\cdot\mathbf{p}$  model of Eq. (2) (solid line) are shown. (b) Nodal lines (red, green and blue) connecting the two TPs (black dots). The grey circles indicate paths for Berry phase calculation. (c) The  $\mathbf{k}\cdot\mathbf{p}$  band structure for the (111)-direction with broken mirror symmetries. Four Weyl points and their chiral charges are shown.

*A novel TSM* — In the inverted band structure the  $\Lambda_6$  and  $\Lambda_{4,5}$  bands cross (see Fig. 3(a)) to form a new type of a TSM. While theoretical evidence for the band inversion in ordered  $\text{InAs}_{0.5}\text{Sb}_{0.5}$  was reported previously [56], the topology of this semimetal phase was overlooked.

Here the crossings are protected by the  $C_3$ -rotational symmetry. For inversion-symmetric materials  $C_3$  is known to stabilize Dirac points on the high-symmetry axis [3, 33, 34]. The inversion symmetry is absent in  $\text{InAs}_{0.5}\text{Sb}_{0.5}$ , so that two of the four bands that would form a Dirac point are gapped. Along the (111)-axis, the two singly degenerate bands  $\Lambda_{4,5}$  each cross with the doubly degenerate  $\Lambda_6$  forming triply degenerate crossings, or triple points (TPs). In the other two directions each TP splits into two linearly dispersing bands and a quadratically dispersing one (see Fig. 3(a)). Previously, TPs have been discussed in the context of Bernal-stacked graphite with neglected SOI [57–59], spin-1 quasiparticles in two dimensions [60, 61] and strained HgTe [62]. The TP we find is furthermore accompanied by four Weyl nodal lines [63] in the vertical mirror planes, degenerate lines between the second and third band in Fig. 3(a), each protected by a Berry phase of  $\pi$  (see Fig. 3(b)).

$E_0$ (meV)	$A$ (eV $\text{\AA}$ )	$B$ (eV $\text{\AA}$ )
0.88	-0.42	4.22
$C$ (eV $\text{\AA}$ )	$D$ (eV $\text{\AA}$ )	$F$ (eV $\text{\AA}$ )
0.78	$1.25 - i1.51$	2.14

TABLE I. Parameters of the fitted  $\mathbf{k}\cdot\mathbf{p}$  model.

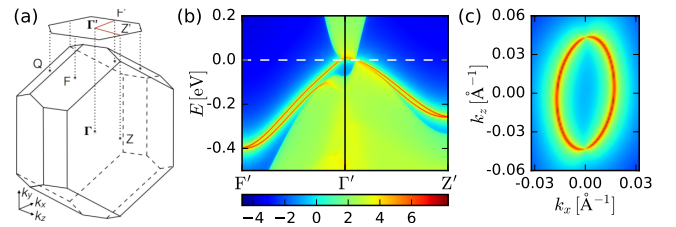


FIG. 4. (a) Brillouin zone and surface projection of CuPt-ordered  $\text{InAs}_{0.5}\text{Sb}_{0.5}$ . (b) Surface density of states for the (110) surface. (c) Topological Fermi arcs on the (110) surface.

In the vicinity of the crossing point the band structure can be described by the following  $\mathbf{k}\cdot\mathbf{p}$  model (see Supplementary Material [51])

$$H_{\mathbf{k}\cdot\mathbf{p}} = \begin{pmatrix} E_0 + Ak_z & 0 & D k_y & D k_x \\ 0 & -E_0 + Ak_z & F^* k_x & -F^* k_y \\ D^* k_y & F k_x & Bk_z + Ck_x & C k_y \\ D^* k_x & -F k_y & C k_y & Bk_z - Ck_x \end{pmatrix}. \quad (2)$$

For  $\text{InAs}_{0.5}\text{Sb}_{0.5}$  the values of the parameters obtained from fits to the first-principles calculations are listed in Tab. I, and the fit is shown in Fig. 3(a). The momentum ( $k_x, k_y, k_z$ ) here is given relative to the crossing point  $\mathbf{k}_c = (0, 0, k_c = 0.0646 \text{\AA}^{-1})$ , and  $k_z$  is taken to be in the (111)-direction and  $k_y$  in the  $(1\bar{1}0)$ -direction.

While a detailed description and topological classification of this novel TSM phase will be provided elsewhere [64], we outline the proof of the topological origin of this phase here. An illustrative verification of the topological origin of this phase is obtained by breaking the mirror symmetry  $\sigma_v$  of the  $C_{3v}$  group. The doubly degenerate band  $\Lambda_6$  splits into two bands, and four crossings are formed as shown in Fig. 3(c). All the four crossings represent Weyl points, with their chiral charges shown in the figure [51]. On the other hand, if all inversion symmetry breaking terms are tuned to zero one obtains a Dirac TSM and thus the TP TSM can be seen as an interpolation of Dirac and Weyl TSMs.

The presence of Dirac or Weyl points in the bulk spectrum of metals is associated with the appearance of Fermi arcs in the surface spectrum [33, 35, 65–69]. Fig. 4 shows the surface density of states, obtained by the iterative Green’s function method [70]. Topological surface states forming the two Fermi arcs that connect the two pairs of TPs at opposite  $\mathbf{k}$  are clearly visible, similar to the ones found in Dirac TSMs. Furthermore, we show in the Supplementary Material [51] that the Landau level spectrum is gapless for a magnetic field aligned parallel to the symmetry axis, hinting at anomalous transport in the presence of magnetic fields [9–11].

*Optimizing the structure for MZMs* — Having established the existence of a novel TSM phase in  $\text{InAs}_{0.5}\text{Sb}_{0.5}$ , we now return to our original purpose of finding an optimal structure for MZM realization. Upon breaking the  $C_3$  symmetry by strain (e.g. (001)-strain) the degeneracy

at the TPs is lifted and the system becomes a semiconductor. The inverted band structure makes it a strong 3D TI in this case, as verified by computing the  $\mathbb{Z}_2$  topological invariant [71]. Figure 5 (a) shows the HSE06 band structure for 1% compressive strain in (001) direction, when all the symmetries of the  $C_{3v}$  structure are broken. In this configuration MZMs can appear in proximitized wires of TIs as discussed by several works [72, 73].

The ordinary band ordering in CuPt-ordered  $\text{InAs}_{0.5}\text{Sb}_{0.5}$  can be restored by applying a symmetry-preserving compressive (111)-strain of  $>2\%$ . Such strain values are easily achievable in nanowires due to lattice mismatch [74, 75]. Moreover, epitaxial semi-super  $\text{InAs}/\text{Al}$  nanowires were reported to bend during the growth process, thus being naturally strained asymmetrically along the (111) growth direction [76].

The HSE06 band structure of (111)-strained  $\text{InAs}_{0.5}\text{Sb}_{0.5}$  is shown in Fig. 5(b) for a 3% strain. In this case the conduction bands acquire a sizable linear in  $k$  SOS in any direction but (111) (see Tab. II). We find that the Rashba coefficient  $\alpha$  is significantly larger than that reported for pristine  $\text{InSb}$  nanowires [27], and the corresponding  $E_{\text{SO}}$  can reach values up to 24 meV, as illustrated in Fig. 6(a) and Tab. II. Note, that the SOS considered here is bulk only and will additionally contribute to the Rashba splitting appearing in a confined geometry.

From Tab. II one can see that  $E_{\text{SO}}$  is large for all the directions orthogonal to the  $C_3$ -axis. Thus, an optimal SOS is achieved in wires grown in the plane of CuPt-structure atomic layers. This suggests gate-defined wires [77] in (111) thin films of  $\text{InAs}_{0.5}\text{Sb}_{0.5}$  to be the most advantageous route to increased stability of MZMs. Additionally, the confinement of the quantum well in the (111) direction has a similar effect as strain and can restore the normal band order for thin quantum wells as is the case in  $\text{HgTe}$  quantum-wells [78].

To give a rough estimate for the realistic value of a TSC gap induced in  $\text{InAs}_{0.5}\text{Sb}_{0.5}$ , we used the obtained parameters in the effective model analysis of Ref. [79] to

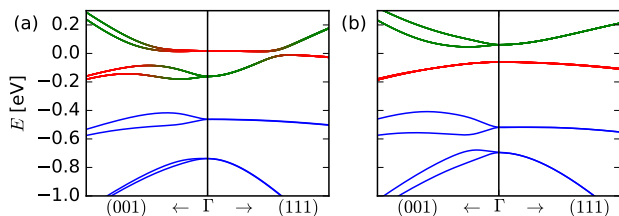


FIG. 5. Valence and conduction energy bands near the  $\Gamma$  point, plotted up to  $|\mathbf{k}| = 0.1 \text{ \AA}^{-1}$ , for CuPt-ordered  $\text{InAs}_{0.5}\text{Sb}_{0.5}$  under strain. The colors correspond to the original band ordering of Fig. 1. (a) 1% compressive strain in the (001)-direction. (b) 3% compressive strain applied in the (111)-direction.

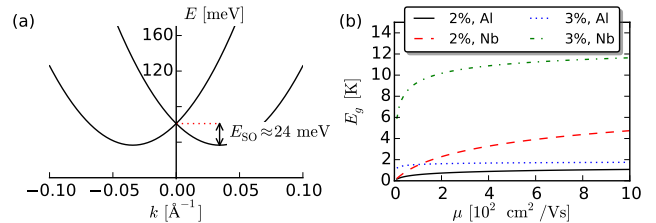


FIG. 6. (a) Conduction bands of  $-3\%$  strained  $\text{InAs}_{0.5}\text{Sb}_{0.5}$  plotted in the  $(1\bar{1}0)$  direction. (b) Disorder renormalized quasiparticle gap  $E_g$  in the TSC state as a function of the mobility plotted for 2% and 3% strain for a  $(1\bar{1}0)$  wire in proximity to Al or Nb.

calculate the disorder renormalized quasiparticle gap  $E_g$  in the TSC state. The gap values  $\Delta_s$  in the adjacent bulk superconductor are taken to be 2 K for Al and 15 K for Nb. In Fig. 6(b)  $E_g$  is plotted as a function of the mobility  $\mu$ , and Tab. II lists values of  $E_g$  assuming Al as the bulk superconductor and a mobility of  $\mu = 10^3 \text{ cm}^2/\text{Vs}$ . Even with this moderate electron mobility  $E_g$  is almost an order of magnitude larger in  $\text{InAs}_{0.5}\text{Sb}_{0.5}$  than what is currently achievable in pure  $\text{InSb}$  [27].

Finally, we considered other III-V alloys, for which CuPt-ordering was reported in Ref. [38]. We found that  $\text{InP}_{0.5}\text{Sb}_{0.5}$  and  $\text{GaAs}_{0.5}\text{Sb}_{0.5}$  realize the novel TSM phase reported above for  $\text{InAs}_{0.5}\text{Sb}_{0.5}$ . Of the compounds with normal band ordering  $\text{Al}_{0.5}\text{Ga}_{0.5}\text{As}$  and  $\text{Al}_{0.5}\text{In}_{0.5}\text{Sb}$  exhibit the largest values of  $E_{\text{SO}}$ , which is small compared to  $\text{InAs}_{0.5}\text{Sb}_{0.5}$ , being of order 0.1 meV [51].

*Acknowledgments.* We would like to thank C. M. Mar-

Material		(111)	(110)	(001)	(1 $\bar{1}0$ )	(11 $\bar{2}$ )
$\text{InAs}_{0.5}\text{Sb}_{0.5}$ -2% (111)-strain	$\alpha$ [eV $\text{\AA}$ ]	0.0	0.8	1.0	1.1	1.0
	$E_{\text{SO}}$ [meV]	0.0	2.7	3.4	3.5	3.5
	$m^*$ [ $m_e$ ]	0.24	0.16	0.14	0.12	0.13
	$l_{\text{R}}$ [ $\text{\AA}$ ]	$\infty$	60	55	60	60
	$ g $	115	95	65	194	177
	$E_g$ [K]	0.0	1.0	1.1	1.1	1.1
$\text{InAs}_{0.5}\text{Sb}_{0.5}$ -3% (111)-strain	$\alpha$ [eV $\text{\AA}$ ]	0.0	0.8	1.2	1.4	1.4
	$E_{\text{SO}}$ [meV]	0.0	6	14	24	24
	$m^*$ [ $m_e$ ]	0.47	0.37	0.41	0.47	0.50
	$l_{\text{R}}$ [ $\text{\AA}$ ]	$\infty$	25	16	11	11
	$ g $	83	69	47	164	161
	$E_g$ [K]	0.0	1.5	1.7	1.7	1.8

TABLE II. Linear coefficient  $\alpha$  of Eq. (1) and  $E_{\text{SO}}$  for different  $k$ -space directions in the CuPt-ordered compound. The spin-orbit precession length  $l_{\text{R}} = \hbar^2/m^*\alpha$  and the Landé  $g$ -factor, for magnetic field parallel to a gate-defined wire in a thin film of 50 nm thickness [51], is also shown.  $E_g$  is calculated using Al as the bulk superconductor and assuming a mobility of  $\mu = 10^3 \text{ cm}^2/\text{Vs}$ .

cus, M. Wimmer and D. Gresch for useful discussions. G. W. W. wants to thank specifically T. Hyart for a correction and useful discussions. This work was supported by Microsoft Research, the European Research Council through ERC Advanced Grant SIMCOFE, and the Swiss National Science Foundation through the National Competence Centers in Research MARVEL and QSIT.

- 
- [1] M. Z. Hasan and C. L. Kane, *Rev. Mod. Phys.* **82**, 3045 (2010).
- [2] X.-L. Qi and S.-C. Zhang, *Rev. Mod. Phys.* **83**, 1057 (2011).
- [3] A. M. Turner and A. Vishwanath, ArXiv e-prints (2013), [arXiv:1301.0330 \[cond-mat.str-el\]](https://arxiv.org/abs/1301.0330).
- [4] X. Wan, A. M. Turner, A. Vishwanath, and S. Y. Savrasov, *Phys. Rev. B* **83**, 205101 (2011).
- [5] Z. Wang, H. Weng, Q. Wu, X. Dai, and Z. Fang, *Phys. Rev. B* **88**, 125427 (2013).
- [6] Z. K. Liu, J. Jiang, B. Zhou, Z. J. Wang, Y. Zhang, H. M. Weng, D. Prabhakaran, S.-K. Mo, H. Peng, P. Dudin, T. Kim, M. Hoesch, Z. Fang, X. Dai, Z. X. Shen, D. L. Feng, Z. Hussain, and Y. L. Chen, *Nat Mater* **13**, 677 (2014).
- [7] G. Volovik, *The Universe in a Helium Droplet*, International Series of Monographs on Physics (OUP Oxford, 2009).
- [8] M. Leijnse and K. Flensberg, *Semiconductor Science and Technology* **27**, 124003 (2012).
- [9] H. Nielsen and M. Ninomiya, *Nuclear Physics B* **185**, 20 (1981).
- [10] P. Hosur and X. Qi, *Comptes Rendus Physique* **14**, 857 (2013).
- [11] D. T. Son and B. Z. Spivak, *Phys. Rev. B* **88**, 104412 (2013).
- [12] D. A. Ivanov, *Phys. Rev. Lett.* **86**, 268 (2001).
- [13] N. Read and D. Green, *Phys. Rev. B* **61**, 10267 (2000).
- [14] S. Nadj-Perge, I. K. Drozdov, J. Li, H. Chen, S. Jeon, J. Seo, A. H. MacDonald, B. A. Bernevig, and A. Yazdani, *Science* **346**, 602 (2014).
- [15] R. M. Lutchyn, J. D. Sau, and S. Das Sarma, *Phys. Rev. Lett.* **105**, 077001 (2010).
- [16] Y. Oreg, G. Refael, and F. von Oppen, *Phys. Rev. Lett.* **105**, 177002 (2010).
- [17] J. Alicea, *Phys. Rev. B* **81**, 125318 (2010).
- [18] J. Alicea, *Reports on Progress in Physics* **75**, 076501 (2012).
- [19] V. Mourik, K. Zuo, S. M. Frolov, S. R. Plissard, E. P. A. M. Bakkers, and L. P. Kouwenhoven, *Science* **336**, 1003 (2012).
- [20] A. Kitaev, *Annals of Physics* **303**, 2 (2003).
- [21] C. Nayak, S. H. Simon, A. Stern, M. Freedman, and S. Das Sarma, *Rev. Mod. Phys.* **80**, 1083 (2008).
- [22] A. Das, Y. Ronen, Y. Most, Y. Oreg, M. Heiblum, and H. Shtrikman, *Nat Phys* **8**, 887 (2012).
- [23] M. T. Deng, C. L. Yu, G. Y. Huang, M. Larsson, P. Caroff, and H. Q. Xu, *Nano Letters* **12**, 6414 (2012).
- [24] S. M. Albrecht, A. P. Higginbotham, M. Madsen, F. Kuemmeth, T. S. Jespersen, J. Nygård, P. Krogstrup, and C. M. Marcus, *Nature* **531**, 206 (2016).
- [25] G. Dresselhaus, *Phys. Rev.* **100**, 580 (1955).
- [26] Y. A. Bychkov and E. Rashba, *JETP Letter* **39**, 78 (1984).
- [27] I. van Weperen, B. Tarasinski, D. Eeltink, V. S. Pribiag, S. R. Plissard, E. P. A. M. Bakkers, L. P. Kouwenhoven, and M. Wimmer, *Phys. Rev. B* **91**, 201413 (2015).
- [28] A. A. Soluyanov, D. Gresch, M. Troyer, R. M. Lutchyn, B. Bauer, and C. Nayak, *Phys. Rev. B* **93**, 115317 (2016).
- [29] M. S. Bahrany, R. Arita, and N. Nagaosa, *Phys. Rev. B* **84**, 041202 (2011).
- [30] S. Picozzi, *Condensed Matter Physics* **2**, 10 (2014).
- [31] Z. Zhu, Y. Cheng, and U. Schwingenschlögl, *New Journal of Physics* **15**, 023010 (2013).
- [32] S. V. Eremeev, I. A. Nechaev, Y. M. Koroteev, P. M. Echenique, and E. V. Chulkov, *Phys. Rev. Lett.* **108**, 246802 (2012).
- [33] Z. Wang, Y. Sun, X.-Q. Chen, C. Franchini, G. Xu, H. Weng, X. Dai, and Z. Fang, *Phys. Rev. B* **85**, 195320 (2012).
- [34] B.-J. Yang and N. Nagaosa, *Nat Commun* **5** (2014).
- [35] Z. Wang, H. Weng, Q. Wu, X. Dai, and Z. Fang, *Phys. Rev. B* **88**, 125427 (2013).
- [36] The definition of  $E_{SO}$  is given in Fig. 6(a).
- [37] H. R. Jen, K. Y. Ma, and G. B. Stringfellow, *Applied Physics Letters* **54**, 1154 (1989).
- [38] G. B. Stringfellow and G. S. Chen, *Journal of Vacuum Science & Technology B* **9**, 2182 (1991).
- [39] S. R. Kurtz, L. R. Dawson, R. M. Biefeld, D. M. Follstaedt, and B. L. Doyle, *Phys. Rev. B* **46**, 1909 (1992).
- [40] D. Ercolani, M. Gemmi, L. Nasi, F. Rossi, M. Pea, A. Li, G. Salviati, F. Beltram, and L. Sorba, *Nanotechnology* **23**, 115606 (2012).
- [41] G. Belenky, Y. Lin, L. Shterengas, D. Donetsky, G. Kipshidze, and S. Suchalkin, *Electronics Letters* **51**, 1521 (2015).
- [42] The virtual crystal approximation [80] (VCA), which is a standard approximation for simulating alloying, is not able to reproduce experimentally known features of  $\text{InAs}_{1-x}\text{Sb}_x$ , such as the nonlinear bowing of the fundamental energy gap  $E_0$  and the spin-orbit gap  $\Delta_0$  (see Fig. 1(a)) [52, 53, 81].
- [43] J. C. Slater and G. F. Koster, *Phys. Rev.* **94**, 1498 (1954).
- [44] P. Vogl, H. P. Hjalmarson, and J. D. Dow, *Journal of Physics and Chemistry of Solids* **44**, 365 (1983).
- [45] G. Klimeck, R. C. Bowen, T. B. Boykin, and T. A. Cwik, *Superlattices and Microstructures* **27**, 519 (2000).
- [46] A. D. Carlo, *Semiconductor Science and Technology* **18**, R1 (2003).
- [47] J. Heyd, G. E. Scuseria, and M. Ernzerhof, *The Journal of Chemical Physics* **118**, 8207 (2003).
- [48] J. Heyd and G. E. Scuseria, *The Journal of Chemical Physics* **121**, 1187 (2004).
- [49] J. Heyd, G. E. Scuseria, and M. Ernzerhof, *The Journal of Chemical Physics* **124**, 219906 (2006).
- [50] Y.-S. Kim, K. Hummer, and G. Kresse, *Phys. Rev. B* **80**, 035203 (2009).
- [51] See Supplementary Information for a detailed description of (additional) first principles calculations, tight-binding models, derivation of  $\mathbf{k} \cdot \mathbf{p}$  models, details on the topological classification and Landé  $g$ -factor calculation.
- [52] S. Cripps, T. Hosea, A. Krier, V. Smirnov, P. Batty, Q. Zhuang, H. Lin, P. Liu, and G. Tsai, *Thin Solid Films* **516**, 8049 (2008).
- [53] S. P. Svensson, W. L. Sarney, H. Hier, Y. Lin, D. Wang,

- D. Donetsky, L. Shterengas, G. Kipshidze, and G. Belenky, *Phys. Rev. B* **86**, 245205 (2012).
- [54] S. Suchalkin, J. Ludwig, G. Belenky, B. Laikhtman, G. Kipshidze, Y. Lin, L. Shterengas, D. Smirnov, S. Luryi, W. L. Sarney, and S. P. Svensson, *Journal of Physics D: Applied Physics* **49**, 105101 (2016).
- [55] Which is the direction of the maximal SOS in pure zincblende semiconductors for small  $k$  [28, 82, 83].
- [56] S. Wei and A. Zunger, *Applied Physics Letters* **58**, 2684 (1991).
- [57] G. P. Mikitik and Y. V. Sharlai, *Low Temperature Physics* **34**, 794 (2008).
- [58] T. T. Heikkilä and G. E. Volovik, *New Journal of Physics* **17**, 093019 (2015).
- [59] T. Hyart and T. T. Heikkilä, *Phys. Rev. B* **93**, 235147 (2016).
- [60] D. Bercioux, D. F. Urban, H. Grabert, and W. Häusler, *Phys. Rev. A* **80**, 063603 (2009).
- [61] D. Green, L. Santos, and C. Chamon, *Phys. Rev. B* **82**, 075104 (2010).
- [62] S. Zaheer, S. M. Young, D. Cellucci, J. C. Y. Teo, C. L. Kane, E. J. Mele, and A. M. Rappe, *Phys. Rev. B* **87**, 045202 (2013).
- [63] A. A. Burkov, M. D. Hook, and L. Balents, *Phys. Rev. B* **84**, 235126 (2011).
- [64] Z. Zhu, G. W. Winkler, Q. Wu, J. Li, and A. A. Soluyanov, *Phys. Rev. X* **6**, 031003 (2016).
- [65] H. Weng, C. Fang, Z. Fang, B. A. Bernevig, and X. Dai, *Phys. Rev. X* **5**, 011029 (2015).
- [66] A. A. Soluyanov, D. Gresch, Z. Wang, Q. Wu, M. Troyer, X. Dai, and B. A. Bernevig, *Nature* **527**, 495 (2015).
- [67] B. Q. Lv, H. M. Weng, B. B. Fu, X. P. Wang, H. Miao, J. Ma, P. Richard, X. C. Huang, L. X. Zhao, G. F. Chen, Z. Fang, X. Dai, T. Qian, and H. Ding, *Phys. Rev. X* **5**, 031013 (2015).
- [68] S.-M. Huang, S.-Y. Xu, I. Belopolski, C.-C. Lee, G. Chang, B. Wang, N. Alidoust, G. Bian, M. Neupane, C. Zhang, S. Jia, A. Bansil, H. Lin, and M. Z. Hasan, *Nat Commun* **6** (2015).
- [69] S.-Y. Xu, C. Liu, S. K. Kushwaha, R. Sankar, J. W. Krizan, I. Belopolski, M. Neupane, G. Bian, N. Alidoust, T.-R. Chang, H.-T. Jeng, C.-Y. Huang, W.-F. Tsai, H. Lin, P. P. Shibayev, F.-C. Chou, R. J. Cava, and M. Z. Hasan, *Science* **347**, 294 (2015).
- [70] M. P. L. Sancho, J. M. L. Sancho, J. M. L. Sancho, and J. Rubio, *Journal of Physics F: Metal Physics* **15**, 851 (1985).
- [71] D. Gresch, M. Troyer, A. Soluyanov, G. Autes, O. Yazyev, A. Bernevig, and D. Vanderbilt, in *APS Meeting Abstracts* (2016).
- [72] A. Cook and M. Franz, *Phys. Rev. B* **84**, 201105 (2011).
- [73] A. M. Cook, M. M. Vazifeh, and M. Franz, *Phys. Rev. B* **86**, 155431 (2012).
- [74] D. Ercolani, F. Rossi, A. Li, S. Roddaro, V. Grillo, G. Salviati, F. Beltram, and L. Sorba, *Nanotechnology* **20**, 505605 (2009).
- [75] M. W. Larsson, J. B. Wagner, M. Wallin, P. Håkansson, L. E. Fröberg, L. Samuelson, and L. R. Wallenberg, *Nanotechnology* **18**, 015504 (2007).
- [76] P. Krogstrup, N. L. B. Ziino, W. Chang, S. M. Albrecht, M. H. Madsen, E. Johnson, J. Nygård, C. M. Marcus, and T. S. Jespersen, *Nat Mater* **14**, 400 (2015).
- [77] J. Reuther, J. Alicea, and A. Yacoby, *Phys. Rev. X* **3**, 031011 (2013).
- [78] B. A. Bernevig, T. L. Hughes, and S.-C. Zhang, *Science* **314**, 1757 (2006).
- [79] J. D. Sau, S. Tewari, and S. Das Sarma, *Phys. Rev. B* **85**, 064512 (2012).
- [80] L. Bellaïche and D. Vanderbilt, *Phys. Rev. B* **61**, 7877 (2000).
- [81] D. J. Chadi, *Phys. Rev. B* **16**, 790 (1977).
- [82] R. Winkler, *Spin-orbit Coupling Effects in Two-Dimensional Electron and Hole Systems*, Springer Tracts in Modern Physics (Springer Berlin Heidelberg, 2003).
- [83] J.-W. Luo, G. Bester, and A. Zunger, *Phys. Rev. Lett.* **102**, 056405 (2009).

# Supplementary Material for "Topological Phases in $\text{InAs}_x\text{Sb}_{1-x}$ : From Novel Topological Semimetal to Majorana Wire"

Georg W. Winkler<sup>1</sup>, QuanSheng Wu<sup>1</sup>, Matthias Troyer<sup>1</sup>, Peter Krogstrup<sup>2</sup>, and Alexey A. Soluyanov<sup>1,3</sup>

<sup>1</sup>Theoretical Physics and Station Q Zurich, ETH Zurich, 8093 Zurich, Switzerland

<sup>2</sup>Center for Quantum Devices and Station Q Copenhagen, Niels Bohr Institute, University of Copenhagen, 2100 Copenhagen, Denmark

<sup>3</sup>Department of Physics, St. Petersburg State University, St. Petersburg, 199034 Russia

Here we provide details on (additional) first principles calculations, tight-binding models, derivation of  $\mathbf{k}\cdot\mathbf{p}$  models, details on the topological classification and Landé  $g$ -factor calculation.

## 1 First-principles simulations

The first-principles calculations were performed in the Vienna *ab initio* simulation package (VASP) [1, 2] with the projector augmented-wave method, using a cut-off energy of 300 eV. The Brillouin zone (BZ) integration was done with Monkhorst-Pack meshes. We used  $8\times 8\times 8$  for pure InAs/InSb,  $6\times 6\times 6$  for CuPt-ordered  $\text{InAs}_{0.5}\text{Sb}_{0.5}$ ,  $6\times 6\times 2$  for 2-layer  $\text{InAs}_{0.67}\text{Sb}_{0.33}/\text{InAs}_{0.33}\text{Sb}_{0.67}$  and a  $4\times 4\times 4$   $k$ -point mesh for the 8 atoms supercells. The later calculation was used for testing the ETB models. The lattice constants for pure InAs and InSb were taken from the work of Ref. [3]. We used VASP pseudopotentials generated with the generalized gradient approximation for the exchange-correlation potential as implemented by Perdew–Burke–Ernzerhof [4]. The HSE06 hybrid functional was employed for all first-principles calculations [5, 6, 7].

During the relaxation the cut-off energy was increased to 380 eV. The relaxed structure for CuPt-ordered  $\text{InAs}_{0.5}\text{Sb}_{0.5}$  is given in Tab. 1. The primitive lattice can be embedded in a nearly cubic superlattice as illustrated in Fig. 1. There the sum  $\mathbf{a}_1 + \mathbf{a}_2 + \mathbf{a}_3$  gives the vertical edge of the cube. Since the  $x$  and  $y$ -component of  $\mathbf{a}_1 + \mathbf{a}_2 + \mathbf{a}_3$  are nonzero the cube is slightly distorted. The 001 and 111 strains were applied such that the volume of the unit cell is preserved.

The total energy per atom of the resulting structure is -4.4432 eV which is in between the energies of pure InAs -4.6458 eV and InSb -4.2900 eV. This hints, together with the experimental evidence [8], at the stability of this ordering.

	$x$ [Å]	$y$ [Å]	$z$ [Å]		$a_1$	$a_2$	$a_3$
$a_1$	-3.1584	0.0000	3.1584	In	-0.0047	-0.0047	0.0140
$a_2$	0.0000	-3.1584	3.1584	In	0.5045	0.5045	0.4865
$a_3$	3.1617	3.1617	6.3200	As	0.8747	0.8747	0.3758
				Sb	0.3755	0.3755	0.8736

Table 1: Lattice vectors and atomic positions in reduced coordinates for the fully relaxed CuPt-ordered InAs<sub>0.5</sub>Sb<sub>0.5</sub>.

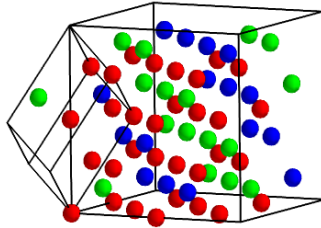


Figure 1: Primitive and cubic unit cells of the CuPt-ordered structure.

Material		(111)	(110)	(001)	(110)	(112)
Al <sub>0.5</sub> Ga <sub>0.5</sub> As	$\alpha$ [eV Å]	0.0	0.08	0.11	0.13	0.13
	$E_{\text{SO}}$ [meV]	0.0	0.04	0.07	0.1	0.1
	$m^*$ [ $m_e$ ]	0.34	0.28	0.24	0.21	0.21
	$l_{\text{R}}$ [Å]	$\infty$	360	290	270	270
	$E_g$ [K]	0.0	0.01	0.02	0.03	0.03
Al <sub>0.5</sub> In <sub>0.5</sub> As	$\alpha$ [eV Å]	0.0	0.07	0.09	0.11	0.11
	$E_{\text{SO}}$ [meV]	0.0	0.02	0.04	0.06	0.06
	$m^*$ [ $m_e$ ]	0.24	0.21	0.18	0.17	0.17
	$l_{\text{R}}$ [Å]	$\infty$	660	440	400	400
	$E_g$ [K]	0.0	0.002	0.006	0.01	0.01

Table 2: Linear spin splitting coefficient  $\alpha$  and  $E_{\text{SO}}$  for different  $k$ -space directions for the CuPt-ordered compounds without strain. The spin-orbit precession length  $l_{\text{R}} = \hbar^2/m^*\alpha$  is also shown.  $E_g$  is calculated using Al as the bulk superconductor and assuming a mobility of  $\mu = 10^3 \text{ cm}^2/\text{Vs}$ .

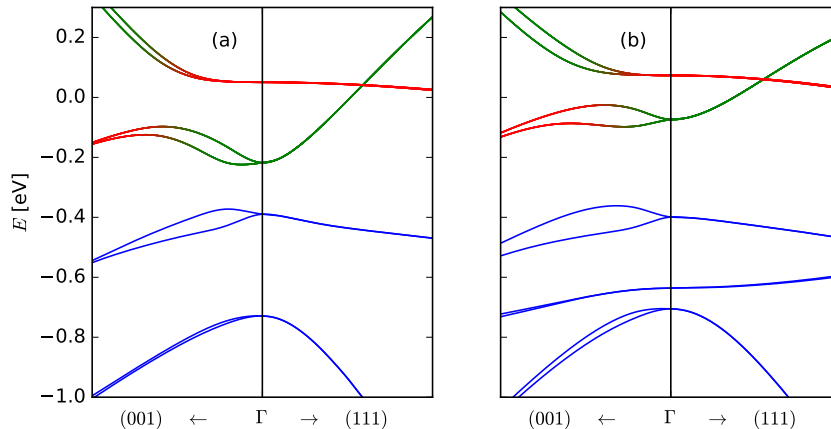


Figure 2: Band structures (HSE06) of the CuPt-ordered  $\text{InAs}_{0.67}\text{Sb}_{0.33}$  (a) and  $\text{InAs}_{0.33}\text{Sb}_{0.67}$  (b).

	$E(s, a)$	$E(s, c)$	$E(p, a)$	$E(p, c)$	$E(s^*, a)$	$E(s^*, c)$	$V(s, s)$	$V(x, x)$
InAs	-9.6858	-2.8259	0.9577	3.7241	7.4099	6.6101	-5.8235	1.8886
InSb	-7.3190	-2.8259	1.0134	3.7241	6.9969	6.6101	-5.7081	1.2220
	$V(x, y)$	$V(sa, pc)$	$V(sc, pa)$	$V(s^*a, pc)$	$V(pa, s^*c)$	$V(s^*, s^*)$	$\Delta_a$	$\Delta_c$
InAs	4.6528	4.0628	5.0267	3.9630	3.0000	0.0000	0.4000	0.3920
InSb	4.0639	4.6255	4.5736	3.0636	3.0000	0.0000	0.8000	0.3920

Table 3: ETB parameters for InAs and InSb in Slater-Koster notation.

In Tab. 2 we show spin-splitting and related quantities for the CuPt-ordered compounds  $\text{Al}_{0.5}\text{Ga}_{0.5}\text{As}$  and  $\text{Al}_{0.5}\text{In}_{0.5}\text{Sb}$ , which have normal band ordering at zero strain and exhibit the largest values of  $E_{\text{SO}}$ . For the first-principles simulations we used the same parameters as for  $\text{InAs}_{0.5}\text{Sb}_{0.5}$  given above.

We tested the stability of the band inversion in CuPt-ordered  $\text{InAs}_x\text{Sb}_{1-x}$  to disorder in the ordering of layers. For  $x = 0.33$  (two As-layers and one Sb-layer) and  $x = 0.67$  (one As-layer and two Sb-layers), there is still a strong band inversion as shown in Fig. 2.

## 2 Empirical tight-binding calculations for disordered $\text{InAs}_x\text{Sb}_{1-x}$

The parameters for the empirical tight-binding (ETB) models used in the main text are listed in Tab. 3 using the Slater-Koster notation [9]. The parameters were obtained by fitting the ETB band structure to the first-principles band structure. To ensure that the tight-binding parametrizations of InAs and InSb are compatible the In atom was described universally, so that In has the same onsite energies in both InAs and InSb ETBs. Figure 3 shows a good agreement between the ETB bands compared to the first-principles result.

ETB results of small disorder configurations in an 8 atoms cubic supercell were compared versus first-principles calculations, and found to be in good

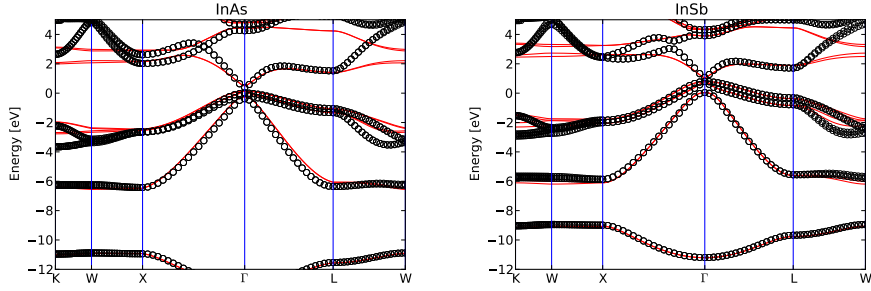


Figure 3: Comparison of ETB (solid red lines) and HSE06 (black open circles) ab initio band structures.

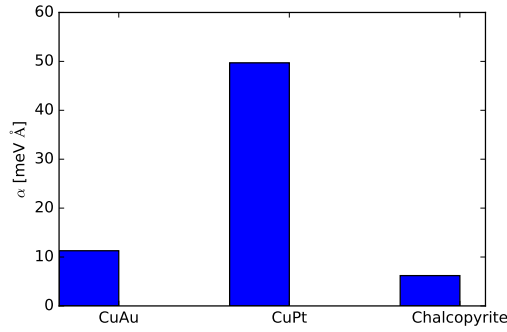


Figure 4: Rashba coefficient  $\alpha$  in the (001)-direction of ordered superstructures in  $\text{InAs}_{0.5}\text{Sb}_{0.5}$ .

agreement. For the supercell sizes shown in Fig. 1(e-d) of the main text we then used ETB calculations only. For each supercell size 31 Sb concentrations were simulated. Every Sb concentration was averaged between 1000 (for 64 atoms supercell) and 20 (for 1728 atoms supercell) random supercell configurations. The energy gap  $E_0$  is plotted for the largest disorder configuration (1728 atoms) and shows negligible dependence on supercell size. The spin-orbit gap  $\Delta_0$  is plotted from the 216 atoms supercell, since for larger supercells band folding makes an identification of the correct gap difficult.  $\Delta_0$  also shows negligible size dependence between the 8, 64 and 216 atoms supercell. The absolute value of the Rashba coefficient  $\alpha$  was extracted from a third order polynomial fit using six data points between  $k = 0$  and  $0.05 \text{ \AA}^{-1}$  in the 110 direction. Then  $\alpha$  was averaged over disorder configurations.

Apart from the disorder simulations, the ETB models were also used to simulate and analyze different ordered supercells. In Fig. 4 we compare the CuAu-, CuPt- and chalcopyrite-ordering in terms of spin-splitting along the (001) direction. The CuPt-type ordering shows the most promising spin-splitting of these structures.

	$\sigma_v$	$C_3$	TR
action on $\mathbf{k}$	$\begin{pmatrix} 1 & & \\ & -1 & \\ & & 1 \end{pmatrix}$	$\begin{pmatrix} -\frac{1}{2} & -\frac{\sqrt{3}}{2} & \\ \frac{\sqrt{3}}{2} & -\frac{1}{2} & \\ & & 1 \end{pmatrix}$	$\begin{pmatrix} -1 & & \\ & -1 & \\ & & -1 \end{pmatrix}$
representation $R$	$\begin{pmatrix} -i & & \\ & i & \\ & & i \end{pmatrix}$	$\begin{pmatrix} -1 & & \\ & -1 & \\ & & \frac{1}{2} & -\frac{\sqrt{3}}{2} \\ & & \frac{\sqrt{3}}{2} & \frac{1}{2} \end{pmatrix}$	$\begin{pmatrix} 0 & \frac{1-i}{\sqrt{2}} & \\ \frac{-1+i}{\sqrt{2}} & 0 & \\ & & 0 & -1 \\ & & 1 & 0 \end{pmatrix} \mathcal{K}$

Table 4: Symmetries and representations of the  $C_{3v}$  double group.  $\mathcal{K}$  is the complex conjugation operator.

### 3 $\mathbf{k} \cdot \mathbf{p}$ models

A  $\mathbf{k} \cdot \mathbf{p}$  description of the crossing point is obtained from group theoretical considerations. First, the representations of the symmetries need to be found. The point group at the crossing point is  $C_{3v}$ , therefore we need to consider the  $C_3$  and  $\sigma_v$  symmetries. In the following we assume  $z$  to be the threefold rotation axis and  $xz$  to be the mirror plane. In Tab. 4 we list the symmetries and their representations. It is easy to check that these representations fulfill the expected relations for spin- $\frac{1}{2}$  particles, e.g.  $(C_3)^3 = (\sigma_v)^2 = -\mathbf{1}$  and they commute with the time-reversal (TR) operator.

Let us first construct a  $\mathbf{k} \cdot \mathbf{p}$  description around the crossing point at  $\mathbf{k}_c = (0, 0, 0.0646) [\text{\AA}^{-1}]$ . The Hamiltonian has to be symmetric under the symmetries of the little group  $(\sigma_v, C_3)$ , that is

$$\begin{aligned} H(\sigma_v \cdot \mathbf{k}) &= R_{\sigma_v} H(\mathbf{k}) R_{\sigma_v}^\dagger, \\ H(C_3 \cdot \mathbf{k}) &= R_{C_3} H(\mathbf{k}) R_{C_3}^\dagger. \end{aligned}$$

Under the above constrains, to linear order in  $\mathbf{k}$ , the Hamiltonian is given by

$$H_{\mathbf{k}\cdot\mathbf{p}} = \begin{pmatrix} E_0 + A_1 k_z & 0 & D k_y & D k_x \\ 0 & -E_0 + A_2 k_z & F^* k_x & -F^* k_y \\ D^* k_y & F k_x & B k_z + C k_x & C k_y \\ D^* k_x & -F k_y & C k_y & B k_z - C k_x \end{pmatrix}. \quad (1)$$

In the main text it was assumed that  $A_1 = A_2$ , which is not dictated by symmetry but almost perfectly fulfilled in the case of CuPt-ordered InAs<sub>0.5</sub>Sb<sub>0.5</sub>. In Fig. 3(b) of the main text we break the  $\sigma_v$  symmetry via adding a local term of the form

$$\gamma \begin{pmatrix} 0 & 1 & & \\ 1 & 0 & & \\ & & 0 & -i \\ & & i & 0 \end{pmatrix}, \quad (2)$$

where we used  $\gamma = 0.0005$ .

Analogously, a  $\mathbf{k} \cdot \mathbf{p}$  model around the zone center  $\Gamma$  can be constructed. In this case the TR symmetry is also included in the little group. Up to quadratic order in  $\mathbf{k}$ , the Hamiltonian is given by

$$H_{\mathbf{k}\cdot\mathbf{p}}^\Gamma = \begin{pmatrix} \epsilon_1(\mathbf{k}) + A_1 k_z & 0 & \omega B k_y & \omega B k_x \\ 0 & \epsilon_1(\mathbf{k}) - A_1 k_z & -B^* k_x & B^* k_y \\ \omega^* B^* k_y & -B k_x & \epsilon_2(\mathbf{k}) + A_2 k_x & A_2 k_y \\ \omega^* B^* k_x & B k_y & A_2 k_y & \epsilon_2(\mathbf{k}) - A_2 k_x \end{pmatrix}, \quad (3)$$

$E_0$ (eV)	$A_1$ (eV Å)	$A_2$ (eV Å)	$B$ (eV Å)	$C$ (eV Å)	$D$ (eV Å)	$E$ (eV Å)	$F$ (eV Å)
0.1696	0.02	1.26	1.48	-5.86	14.3	-3.91	54.2

Table 5: Parameters of the fitted  $\mathbf{k} \cdot \mathbf{p}$  model around  $\Gamma$ .

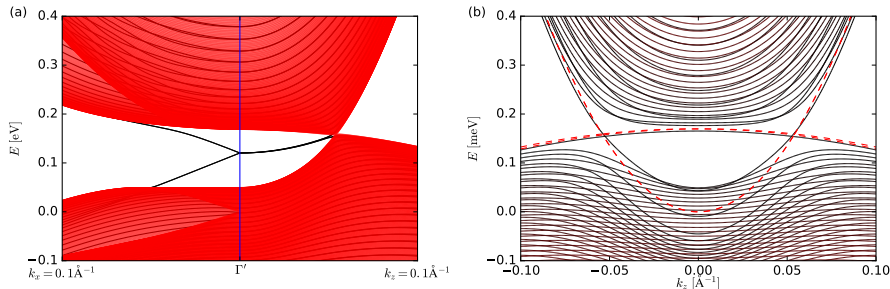


Figure 5: (a) The surface states of the  $\mathbf{k} \cdot \mathbf{p}$ -model given in Eq. (3) in a slab geometry terminated in a  $xz$ -surface. (b) Landau level calculation for a magnetic field of 50 Tesla in the  $z$ -direction. The red dashed line is the original band structure of the  $\mathbf{k} \cdot \mathbf{p}$ -model.

with  $\omega = \frac{1-i}{\sqrt{2}}$  and

$$\begin{aligned}\epsilon_1 &= E_0 + C(k_x^2 + k_y^2) + Ek_z^2 \\ \epsilon_2 &= D(k_x^2 + k_y^2) + Fk_z^2.\end{aligned}$$

If  $A_1$  and  $A_2$  are set to zero inversion symmetry is restored and the model describes a Dirac semimetal. In Tab. 5 we give a set of parameters fitted to our HSE06 first-principles calculations of  $\text{InAs}_{0.5}\text{Sb}_{0.5}$ . By discretizing  $k_y$  (see e.g. Ref. [10]) we calculated the surface states on the  $xz$ -surface in a slab geometry in Fig. 5(a). The qualitative behaviour of the surface states agrees with Fig. 4(a) of the main text. Furthermore, we calculate the Landau level spectrum for a magnetic field of 50 Tesla applied in the  $z$ -direction in Fig. 5(b). We do this by performing a Peierls substitution, replacing  $k_x$  and  $k_y$  in Eq. (3) by the corresponding operators in the presence of magnetic fields (see e.g. Ref. [11] for details). We find two gapless Landau levels crossing, similar to the case of a Dirac semimetal [11].

## 4 Evaluation of the chiral charge

The evaluation of the chiral charge, leading to the results shown in Fig. 3(b) of the main text, is facilitated by measuring the Berry flux through a closed surface containing the semimetallic point(s). We choose the surface to be a sphere, on which the Hamiltonian is gapped. Then the topology of this surface is characterized by a Chern number [12], or can also be characterized by a  $\mathbb{Z}_2$  quantum number if additional symmetries are present [13]. We evaluate the topology by tracking the hybrid Wannier charge centers (see Ref. [14] for further details) using the software package Z2Pack [15].

In Fig. 6 we present the results obtained using the  $\mathbf{k} \cdot \mathbf{p}$ -model of Eq. (1) with  $\sigma_v$  breaking term of the form in Eq. (2) added. In Fig. 6(a) we show the Chern

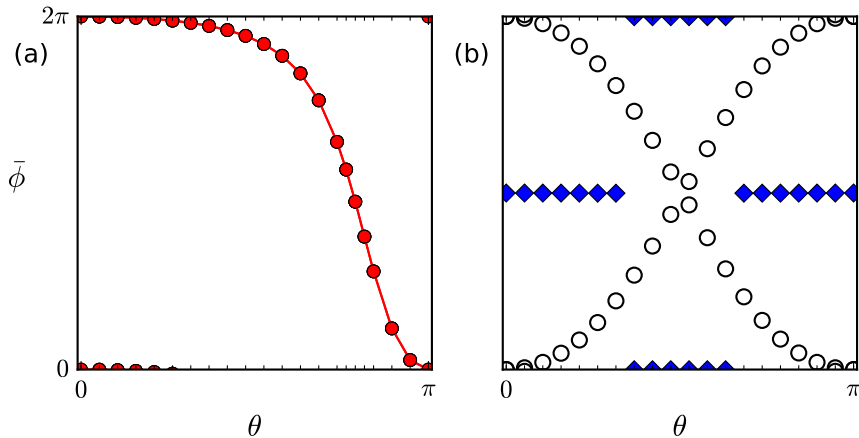


Figure 6: (a) Chern number calculation on a sphere enclosing a single Weyl point with chiral charge -1. (b) Wannier charge centers on a sphere enclosing all four Weyl points.

number calculation for a single Weyl point. Details on the calculation (and the definitions of the labels  $\phi$  and  $\theta$  in Fig. 6(a)) can be found in the supplementary information of Ref. [16].

In Fig. 6(b) the sphere contains all four Weyl points. We set the Fermi level such that two Weyl points contribute to the topological charge, corresponding to the leftmost and rightmost Weyl points in Fig. 3(b) of the main text. Since there are two occupied states two hybrid Wannier centers are shown (open circles) in Fig. 6(b). The crossing of the two hybrid Wannier centers is analogous to a  $Z_2$  invariant of Kane-Mel [13], which is non-trivial in the case shown. This classification can also be used with mirror symmetry and allow for a classification of the triple crossing points. However, both triple crossing points need to be contained in the sphere, otherwise the occupied and unoccupied states are not separated by an energy gap.

## 5 Landé $g$ -factor

In the main text we propose gate-defined wires in thin films of  $\text{InAs}_{0.5}\text{Sb}_{0.5}$ . Here we estimate the Landé  $g$ -factor that can be achieved in such a setup.

We first construct effective tight-binding Hamiltonians generated from first-principles Wannier functions [17], using the  $s$  and  $p$ -like orbitals of In and the  $p$ -like orbitals As and Sb. The Wannier functions are generated without taking spin-orbit interaction into account, which is added afterwards locally to all  $p$ -orbitals [18]. The atomic spin-orbit interaction constants of In, As and Sb were taken from Ref. [18]. We used these tight-binding models then to calculate the band structure of slabs in various directions with various thicknesses. An in-plane magnetic field is added to the tight-binding Hamiltonian using the scheme of Ref. [19]. Due to the orientation of the magnetic field we can choose the electromagnetic gauge such that the vector potential only changes in the direction orthogonal to the slab, thus not breaking the periodicity of the slab.

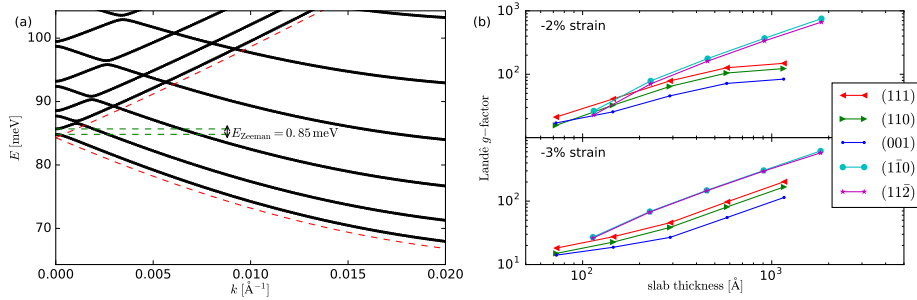


Figure 7: (a) Band structure of a (111)-slab of  $\text{InAs}_{0.5}\text{Sb}_{0.5}$ , with 458 Å thickness, -3% (111) strain and an in-plane magnetic field of 0.1 Tesla in  $(1\bar{1}0)$  direction and  $k$  plotted in the same direction. The red dashed lines are the bulk band structure without the magnetic field. (g) Landé  $g$ -factor of  $\text{InAs}_{0.5}\text{Sb}_{0.5}$  as a function of the slab thickness for the magnetic field in different directions and different strain levels.

In Fig. 7(a) we show the typical band structure of a (111)-slab of  $\text{InAs}_{0.5}\text{Sb}_{0.5}$  at a magnetic field of 0.1 Tesla. The Landé  $g$ -factor is extracted from the Zeeman splitting  $E_{\text{Zeeman}} = \mu_B g B$  of the subband energetically closest to the first bulk conduction band at  $\Gamma$ . For magnetic field in the (111), (110) and (001) direction we use  $(1\bar{1}0)$ -slabs and for the magnetic field in  $(1\bar{1}0)$  and  $(11\bar{2})$  we use (111)-slabs. The  $g$ -factor is evaluated in a magnetic field of  $B = 0.001$  Tesla, ensuring that the Zeeman gap is smaller than the subband gap for all considered slab sizes. The resulting  $g$ -factors as a function of the slab thickness are plotted in Fig. 7(b). The values of the  $g$ -factor at 500 Å thickness were obtained via interpolating between adjacent calculated slab thicknesses.

## References

- [1] G. Kresse and J. Furthmüller, “Efficient iterative schemes for *ab initio* total-energy calculations using a plane-wave basis set,” *Phys. Rev. B*, vol. 54, pp. 11169–11186, Oct 1996.
- [2] G. Kresse and J. Furthmüller, “Efficiency of ab-initio total energy calculations for metals and semiconductors using a plane-wave basis set,” *Computational Materials Science*, vol. 6, no. 1, pp. 15 – 50, 1996.
- [3] G. Giesecke and H. Pfister, “Präzisionsbestimmung der Gitterkonstanten von  $A_{III}B_V$ -Verbindungen,” *Acta Crystallographica*, vol. 11, pp. 369–371, May 1958.
- [4] J. P. Perdew, K. Burke, and M. Ernzerhof, “Generalized gradient approximation made simple,” *Phys. Rev. Lett.*, vol. 77, pp. 3865–3868, Oct 1996.
- [5] J. Heyd, G. E. Scuseria, and M. Ernzerhof, “Hybrid functionals based on a screened Coulomb potential,” *The Journal of Chemical Physics*, vol. 118, no. 18, pp. 8207–8215, 2003.

- [6] J. Heyd and G. E. Scuseria, “Efficient hybrid density functional calculations in solids: Assessment of the Heyd–Scuseria–Ernzerhof screened Coulomb hybrid functional,” *The Journal of Chemical Physics*, vol. 121, no. 3, pp. 1187–1192, 2004.
- [7] J. Heyd, G. E. Scuseria, and M. Ernzerhof, “Erratum: “Hybrid functionals based on a screened Coulomb potential” [j. chem. phys.118, 8207 (2003)],” *The Journal of Chemical Physics*, vol. 124, no. 21, p. 219906, 2006.
- [8] G. B. Stringfellow and G. S. Chen, “Atomic ordering in III/V semiconductor alloys,” *Journal of Vacuum Science & Technology B*, vol. 9, no. 4, pp. 2182–2188, 1991.
- [9] J. C. Slater and G. F. Koster, “Simplified LCAO method for the periodic potential problem,” *Phys. Rev.*, vol. 94, pp. 1498–1524, Jun 1954.
- [10] P. Sengupta, H. Ryu, S. Lee, and Y. Tan, “Numerical guidelines for setting up a general purpose k.p simulator with applications to quantum dot heterostructures and topological insulators,” *ArXiv e-prints*, Sept. 2014.
- [11] S. Jeon, B. B. Zhou, A. Gyenis, B. E. Feldman, I. Kimchi, A. C. Potter, Q. D. Gibson, R. J. Cava, A. Vishwanath, and A. Yazdani, “Landau quantization and quasiparticle interference in the three-dimensional Dirac semimetal  $\text{Cd}_3\text{As}_2$ ,” *Nat Mater*, vol. 13, pp. 851–856, 09 2014.
- [12] D. J. Thouless, M. Kohmoto, M. P. Nightingale, and M. den Nijs, “Quantized Hall conductance in a two-dimensional periodic potential,” *Phys. Rev. Lett.*, vol. 49, pp. 405–408, Aug 1982.
- [13] C. L. Kane and E. J. Mele, “ $Z_2$  topological order and the Quantum Spin Hall effect,” *Phys. Rev. Lett.*, vol. 95, p. 146802, Sep 2005.
- [14] A. A. Soluyanov and D. Vanderbilt, “Computing topological invariants without inversion symmetry,” *Phys. Rev. B*, vol. 83, p. 235401, Jun 2011.
- [15] D. Gresch, M. Troyer, A. Soluyanov, G. Autes, O. Yazyev, A. Bernevig, and D. Vanderbilt, “Universal framework for identifying topological materials and its numerical implementation in z2pack software package,” in *APS Meeting Abstracts*, 2016.
- [16] A. A. Soluyanov, D. Gresch, Z. Wang, Q. Wu, M. Troyer, X. Dai, and B. A. Bernevig, “Type-II Weyl semimetals,” *Nature*, vol. 527, p. 495, Nov. 2015.
- [17] A. A. Mostofi, J. R. Yates, Y.-S. Lee, I. Souza, D. Vanderbilt, and N. Marzari, “wannier90: A tool for obtaining maximally-localised Wannier functions,” *Computer physics communications*, vol. 178, no. 9, pp. 685–699, 2008.
- [18] D. J. Chadi, “Spin-orbit splitting in crystalline and compositionally disordered semiconductors,” *Phys. Rev. B*, vol. 16, pp. 790–796, Jul 1977.
- [19] M. Graf and P. Vogl, “Electromagnetic fields and dielectric response in empirical tight-binding theory,” *Phys. Rev. B*, vol. 51, pp. 4940–4949, Feb 1995.